

PROBING PULSAR SCATTERING BETWEEN 120 AND 280 MHZ WITH THE MWA

F. KIRSTEN,^{1,2} N. D. R. BHAT,² B. W. MEYERS,^{2,3} J.-P. MACQUART,² S. E. TREMBLAY,² AND S. M. ORD³

¹*Department of Space, Earth and Environment, Chalmers University of Technology, Onsala Space Observatory, 439 92, Onsala, Sweden*

²*International Centre for Radio Astronomy Research, Curtin University, Bentley, WA 6102, Australia*

³*CSIRO Astronomy and Space Science, P.O. Box 76, Epping, NSW 1710, Australia*

ABSTRACT

The high sensitivity and wide frequency coverage of the Murchison Widefield Array allow for the measurement of the spectral scaling of the pulsar scattering timescale, α , from a single observation. Here we present three case studies targeted at bright, strongly scattered pulsars J0534+2200 (the Crab pulsar), J0835–4510 (the Vela pulsar) and J0742–2822. We measure the scattering spectral indices to be -3.8 ± 0.2 , -4.0 ± 1.5 , and -2.5 ± 0.6 for the Crab, Vela, and J0742–2822, respectively. We find that the scattered profiles of both Vela and J0742–2822 are best described by a thin screen model where the Gum Nebula likely contributes most of the observed scattering delay. For the Crab pulsar we see characteristically different pulse shapes compared to higher frequencies, for which none of the scattering screen models we explore are found to be optimal. The presence of a finite inner scale to the turbulence can possibly explain some of the discrepancies.

Keywords: pulsars: general — pulsars: individual (PSRs J0534+2200, J0742–2822, J0835–4510) — ISM: structure — scattering

1. INTRODUCTION

The interstellar medium (ISM) is a cold plasma that disperses and scatters pulsar radiation. Dispersion causes the broadband signal of a pulsar to be smeared out in time such that a particular pulse arrives at the observer later in time at lower frequencies than at higher frequencies. This is quantified in terms of the dispersion measure, $DM = \int_0^D n_e(l) dl$, which is the integral over the electron density, n_e , along the line of sight to a pulsar at distance D . Dispersion is generally well understood, with the dispersion delay τ_{dm} scaling as the inverse of the observing frequency ν squared: $\tau_{dm} \propto \nu^{-2}$. Thus, dispersion can be corrected for, modulo the time variability (e.g. Keith et al. 2013; You et al. 2007) and possible chromaticity (Cordes et al. 2016) of the DM. Both dependencies, $DM(t)$ and the suggested $DM(\nu)$, originate in the inhomogeneous, turbulent ISM: the motion of a pulsar relative to the ISM and Earth causes the pulsar signal to probe different parts of the ISM over time. At the same time, density variations in the ISM cause radio waves to be scattered over a range of directions, resulting in an angular spectrum with a characteristic width θ_{scatt} , i.e. the scattering angle. The integrated effect is that an intrinsically narrow pulse becomes broadened in time as off-axis radiation is scattered back into the line of sight and arrives later at the observer due to the extra path length. The measurable effect of scatter broadening, the scattering delay τ , depends on frequency roughly as ν^{-4} .

As such, scattering is the main hindrance to perform accurate pulsar timing at lower frequencies ($\nu \lesssim 1$ GHz) where pulsars tend to be brighter. At the same time this means that high sensitivity observations of pulsars at low radio frequencies are ideal to use both effects and their variation with time and frequency to study the properties of the ISM itself. The shape of a scattered profile and its evolution as a function of frequency give us insights into the underlying geometry, dynamics and physics of the ISM. For example, the shape of the rising edge of a pulse depends on the distribution of the scattering medium along the line of sight, namely whether it is homogeneously distributed or organized in (possibly multiple) thin sheets. Similarly, the detailed structure of the scattering tail reveals the underlying structure function of density irregularities in the ISM (Lambert & Rickett 1999).

Since the impact of the ISM on pulsar radiation is strongest at low frequencies, observations of bright scattered pulsars at $\nu \lesssim 300$ MHz are well suited to differentiating between competing models of the ISM. In particular, it remains unclear whether Kolmogorov turbulence appropriately describes and quantifies variations in

Table 1. Characteristics of the observed pulsars

| Pulsar | Period [ms] | DM [pc cm ⁻³] | Distance [kpc] | (l, b) (°, °) |
|------------|----------------|------------------------------|-------------------|------------------|
| J0534+2200 | 33.3 | 56.7 | 1.31 ^a | (184.5, -5.7) |
| J0742-2822 | 166.7 | 73.7 | 3.11 ^a | (243.7, -2.4) |
| J0835-4510 | 89.3 | 67.9 | 0.28 ^b | (263.5, -2.7) |

NOTE—From the ATNF Pulsar Catalogue, Manchester et al. (2005)

^aDM-derived distance assuming the YMW16 model of Yao et al. (2017)

^bParallax based measurement (Dodson et al. 2003)

DM, the frequency scaling of pulsar scattering, and the scintillation properties of pulsars (e.g. Lam et al. 2016). The parabolic arcs in secondary spectra of scintillating pulsars (e.g. Brisken et al. 2010; Stinebring et al. 2001) disfavor a homogeneous, isotropically distributed scattering medium (e.g. Walker et al. 2004). Instead, they hint at localized, anisotropic scattering structures that could have a sheet like geometry (e.g. Braithwaite 2015; Pen & Levin 2014).

The scattering delay induced by the interstellar medium scales with frequency as $\nu^{-2\beta/(\beta-2)}$, where β is the power spectral index of density irregularities. For Kolmogorov turbulence we expect $\beta = 11/3$ (e.g. Rickett 1990). Most of the published measurements of $\alpha = -2\beta/(\beta-2)$, however, deviate from the theoretically expected value $\alpha = -4.4$. In fact, the majority of recently published measurements obtained from low frequency observations of pulsars list spectral indices $\alpha > -4$ (Geyer et al. 2017; Meyers et al. 2017; Krishnakumar et al. 2017; Eftekhari et al. 2016; Lewandowski et al. 2015). Evidence for shallower scaling also comes from a large sample of pulsar measurements by Bhat et al. (2004), who deduced a value of $\langle\alpha\rangle = -3.9 \pm 0.2$ for the global scattering index. They also offer a possible explanation in terms of an inner scale and a crossover point that depends on this scale. Cordes & Lazio (2001) explain such ‘anomalous’ scattering behavior by introducing filamentary structures along the line of sight; a scenario that can also give rise to shallow scattering. Xu & Zhang (2017) invoke supersonic turbulence and a frequency dependent volume filling factor of density irregularities to reconcile observations and theoretical models. Geyer & Karastergiou (2016) investigate the idea of anisotropic pulse broadening functions in the case of a thin screen, finding that the standard isotropic models can significantly underestimate the scattering time, especially at low frequencies. In a recent study, Geyer et al. (2017) compare spectral

Table 2. Details of the observations

| Pulsar | Observing duration | | Central Frequencies of subbands | Bandwidth per subband |
|------------|--------------------|-----------|--|-----------------------|
| | MJD | [seconds] | [MHz] | [MHz] |
| J0534+2200 | 56968 | 3600 | 120.96, 165.76, 210.56, 278.40 | 7.68 |
| J0742–2822 | 57422 | 300 | 77.44, 149.12, 210.56, 311.68 | 2.56 |
| | | | 87.04, 97.28, 107.52, 117.76, 128.00, 158.72 | 1.28 |
| | | | 168.96, 179.20, 189.44, 199.68, 220.16, | 1.28 |
| | | | 230.40, 271.36, 281.60, 291.84, 302.08 | 1.28 |
| J0835–4510 | 56961 | 1200 | 120.96, 210.56, 256.64 | 7.68 |
| | | | 164.48 | 5.12 |
| | | | 179.84 | 2.56 |

indices obtained by fitting isotropic and anisotropic models to multi-frequency scattering observations, finding that the latter models yield values for α that are in better agreement with theoretical expectations.

Obviously, the ISM cannot be fully described by an isotropic model in which the power spectrum of density irregularities follows a simple power law. In order to shed further light on the physics of the ISM, more detailed studies of the shape and the temporal and spectral evolution of scattered pulsar profiles at low frequencies ($\nu \lesssim 300$ MHz) are required. New instruments such as the Murchison Widefield Array (MWA, [Tingay et al. 2013](#)), the Low Frequency Array (LOFAR, [van Haarlem et al. 2013](#)), and the Long Wavelength Array (LWA, [Taylor et al. 2012](#)) can provide the sensitivity, the frequency coverage, and also the temporal resolution needed for making further progress in this area.

In this work we present a pilot study of pulsar scattering using the MWA. We selected three bright, moderate DM pulsars – J0534+2200, J0742–2822, and J0835–4510 (Table 1) – and observed them across the large frequency range of the MWA (80 – 300 MHz). We show that for bright pulsars the sensitivity of the MWA is sufficient to obtain high quality pulse profiles within a short integration time (~ 5 min), allowing for a measurement of the frequency scaling index α for all three targets from a single observation.

In Section 2 we describe the MWA observations, and in Section 3 we present our results and an analysis of the scattering profiles. Our results are discussed in Section 4 and the conclusions are presented in Section 5.

2. OBSERVATIONS & DATA REDUCTION

We observed the three pulsars J0534+2200 (the Crab pulsar), J0742–2822, and J0835–4510 (the Vela pulsar) with the MWA using the Voltage Capture System (VCS, [Tremblay et al. 2015](#)). This observing mode records the

channelised voltages from each of the 128 tiles¹, which can be summed coherently after performing calibration. In order to be able to characterize the scattering properties of each target we observed in the following manner: instead of observing over a contiguous band of maximal 30.72 MHz bandwidth, we spread the 24 available individual coarse channels across the accessible frequency range of 80 – 300 MHz. Each of these coarse channels has a bandwidth of 1.28 MHz which, before recording, is channelised into 128 fine channels (i.e. 10 kHz) in a polyphase filterbank. Multiple subbands can be constructed by either grouping consecutive coarse channels, or by using individual coarse channels as subbands.

We used different frequency setups for each target as indicated in Table 2. The number of subbands ranged from 4 to 20, hence the bandwidth varied between 1.28 MHz and 7.68 MHz per subband. Observing duration varied from about 5 to 60 minutes depending on the target. For calibration purposes we also performed a short (~ 2 min) observation of a strong nearby calibrator (non-pulsar continuum source) using the same frequency setup as for the respective pulsar prior to the target observations. The calibrator scans were not recorded with the VCS but instead with the MWA correlator ([Ord et al. 2015](#)) which produced visibilities at a cadence of 10 kHz and 2 s.

2.1. Calibration

We performed calibration using the Real Time System (RTS, [Mitchell et al. 2008](#)) which corrects for various instrumental effects and removes positional offsets of sources induced by the refractive ionosphere.

¹ The tiles are about $4\text{ m} \times 4\text{ m}$ in size, comprising 16 dipoles each. At the time of the observations, the majority of the tiles (112) were spread over a 1.5 km core region with the remaining 16 tiles being located at larger distances, allowing for baselines up to 3 km in length.

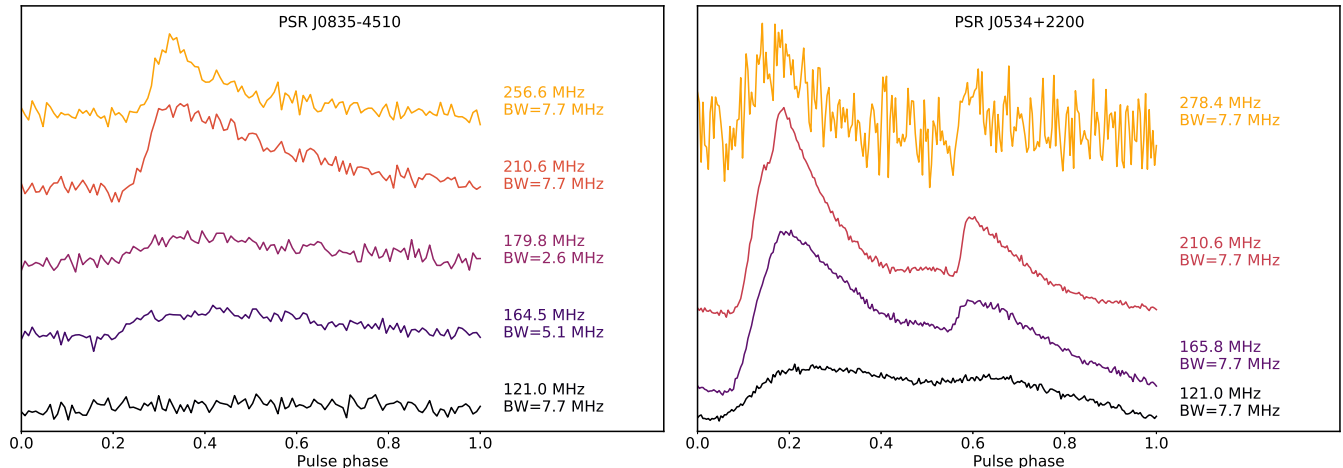


Figure 1. Folded pulse profiles of the Vela pulsar (left) and the Crab pulsar (right) across the MWA-band. We used coherently summed data for frequencies below 235 MHz while we used incoherently summed data for the highest bands (we did not manage to form a coherent beam above 235 MHz because of RFI). For Vela, the bandwidth varies as indicated while for the Crab it is constant at 7.7 MHz. The low signal-to-noise ratio (SNR) for the Crab at 278.4 MHz is due to three factors: the steep spectrum of the pulsar, the amount of RFI in the band, and the reduced sensitivity of the MWA towards the upper end of the band.

The RTS uses a fully polarimetric calibration formalism (Sault et al. 1996) to form a least squares estimate of the complex gain of the constituent antennas in the array. Ionospheric refraction manifests predominantly as a position offset in the direction of the calibrator, and can be extracted from the antenna phase terms as a phase ramp with a quadratic frequency dependence. Thus antenna gain terms are obtained that are direction independent and can be applied to form phased array beams anywhere on the sky.

The RTS generates bandpass calibration solutions and direction-independent Jones Matrices (DIJs). The latter contain full polarization calibration solutions across the entire field of view (FOV) of the MWA (Full Width Half Maximum $\sim 25^\circ$ at 150 MHz) for each of the individual 24 channels. The RTS inherently assumes a contiguous bandpass of 30.72 MHz bandwidth which is not directly applicable in the case of split band observations performed here. It is, however, possible to calibrate individual channels or groups of consecutive channels. We thus used the RTS software package separately for each of the subbands listed in Table 2 using models of the respective calibrators as developed by Line et al. (2016). Typically, the ionosphere is stable enough for one such calibration solution to be valid over several hours.

In the case of the Crab pulsar we did not use the dedicated calibrator observation but instead performed in-field calibration on the target itself. As the RTS performs its analysis on visibilities, we first correlated 200 seconds of the voltages recorded for the Crab pulsar using the standard MWA software correlator.

2.2. Coherent beam-forming

To compute the coherent sum of the signals from all 128 tiles, we use a software package specifically developed for the MWA (Ord et al., in prep., referred to as the ‘beamformer’ below). The full description of the beamformer is beyond the scope of this article but we describe the individual steps here briefly.

When forming the coherent sum of the signals from all tiles the FOV of the MWA is reduced significantly. Between the lower (~ 80 MHz) and the upper (~ 300 MHz) band edges of the instrument, the size of this pencil beam ranges from about $4'$ to about $1'$, which is, effectively, the size of the synthesized beam. To phase up on a particular field of this size within the incoherent FOV, the pencil beam needs to be ‘steered’ towards that desired direction. As the name suggests, the DIJs obtained after running the RTS on the calibrator scan contain no information about a specific direction (i.e. towards a source) within the incoherent FOV of the target scan. Therefore, starting from the DIJs we first compute the geometric phase offsets from the pointing center of the target scans for the direction we would like to form a coherent beam on (i.e. the coordinates of the pulsar). These delays are computed for each 10 kHz wide fine channel on a per-second basis. The complex gains from both the DIJs and the direction-dependent calibration are applied to the raw voltages of the target scans, after which the signals are summed and detected to form a time series of power.

This strategy works provided the RTS converges on a valid calibration solution. In our observations, frequency subbands above ~ 235 MHz were, unfortunately, strongly affected by radio frequency interference (RFI)

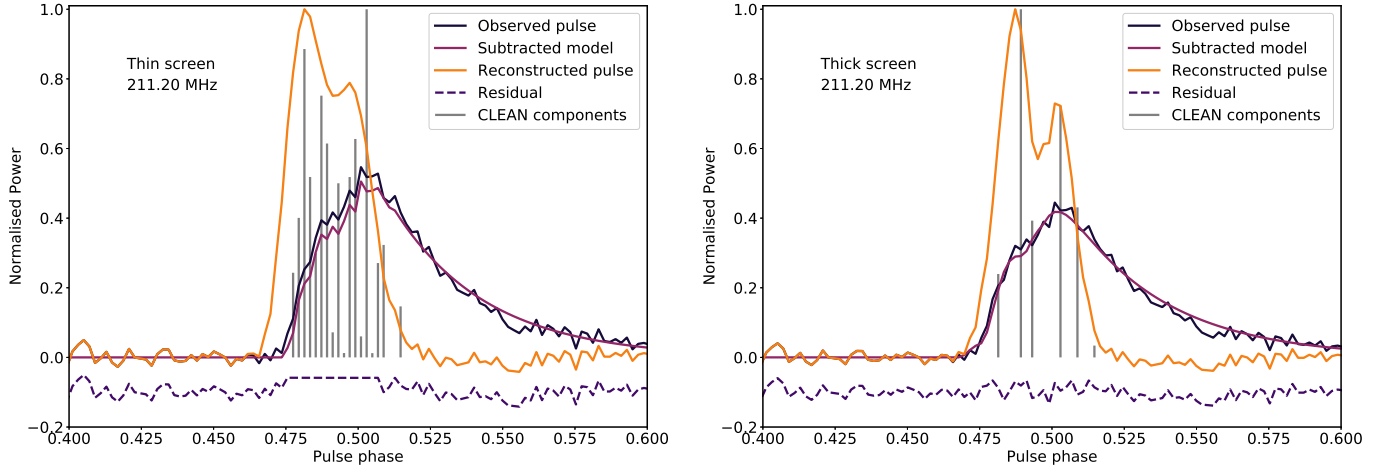


Figure 2. Illustration of the CLEANing process using the example of J0742–2822 at 211.2 MHz for both the thin (left) and thick (right) screen models. The black line shows the observed pulse, the vertical gray lines represent the locations and relative amplitudes of the CLEAN components summed up per phase bin. The purple solid line shows the sum of all CLEAN components that were convolved with the thin/thick screen model and subsequently subtracted from the observed pulse. The residual after subtraction is represented by the purple dashed line and is offset from the origin for illustration purposes. Finally, the yellow line shows the recovered (intrinsic) pulse shape as computed from the CLEAN components convolved with a Gaussian.

generated by satellites. As a result, the RTS failed to provide usable DIJs, thus making a coherent summation of the raw voltages impossible. Therefore we reverted to the incoherently summed voltages² in bands above 235 MHz. As the Crab and Vela were sufficiently bright and integrations times were long, we were able to detect both pulsars even with the MWA’s incoherent sensitivity. For J0742–2822 the integration time and bandwidth were too small to result in a detection in this upper frequency range using the incoherently summed data.

3. ANALYSIS & RESULTS

We used the software packages PSRCHIVE (Hotan et al. 2004; van Straten et al. 2012) and DSPSR (van Straten & Bailes 1997) for further data processing and analysis. We processed the individual subbands for each pulsar separately, and the resultant, incoherently dedispersed pulse profiles are shown in Figures 1 and 3.

One of our main goals is to quantify the physical nature of scattering along the sight lines to the three different pulsars. To that end, we explore different pulse broadening functions (PBFs) to fit the observed pulse profiles in each band and measure the frequency scaling of the scattering delay τ . However, for a least-squares fitting procedure to be easily applicable, the intrinsic pulse shape needs to be known with high accuracy and the characteristic scattering time needs to be small

enough that the scattering tail does not extend beyond the pulsar period. In practice, this need not necessarily be the case; measured profiles can be composed of multiple components whose shapes and separations cannot be easily extrapolated to low frequencies from higher frequency observations. Moreover, long scattering tails result in an apparent merging of the components and render the determination of a baseline impossible. In the case of the Crab pulsar this is alleviated by analyzing individual giant pulses (e.g. Meyers et al. 2017; Bhat et al. 2007).

For the other two pulsars we employ a deconvolution technique based on the CLEAN algorithm (Högbom 1974) which was implemented for pulse profiles by Bhat et al. (2003). The method recovers an intrinsic pulse shape by deconvolving the observed profile with an assumed model of the PBF (Fig. 2), nonetheless trialling over a range of τ to determine the best-fit value. Two commonly adopted models are a thin screen model and a thick screen model.

In general, the exact form of the PBF associated with the ISM is unknown and depends on the distribution and the turbulence power spectrum of the scattering material along the line of sight to the pulsar. Assuming a square-law structure function for density inhomogeneities, the simplest PBF for a thin screen model is a one-sided exponential,

$$g_0(t) = \left(\frac{1}{\tau}\right) \exp\left[-\frac{t}{\tau}\right] u(t), \quad (1)$$

where $u(t < 0) = 0$ and $u(t \geq 0) = 1$.

² For the incoherent sum we detect the signal per tile and then sum the time series of power. This reduces the sensitivity (compared to the coherent beam) by a factor \sqrt{N} , where N is the number of tiles.

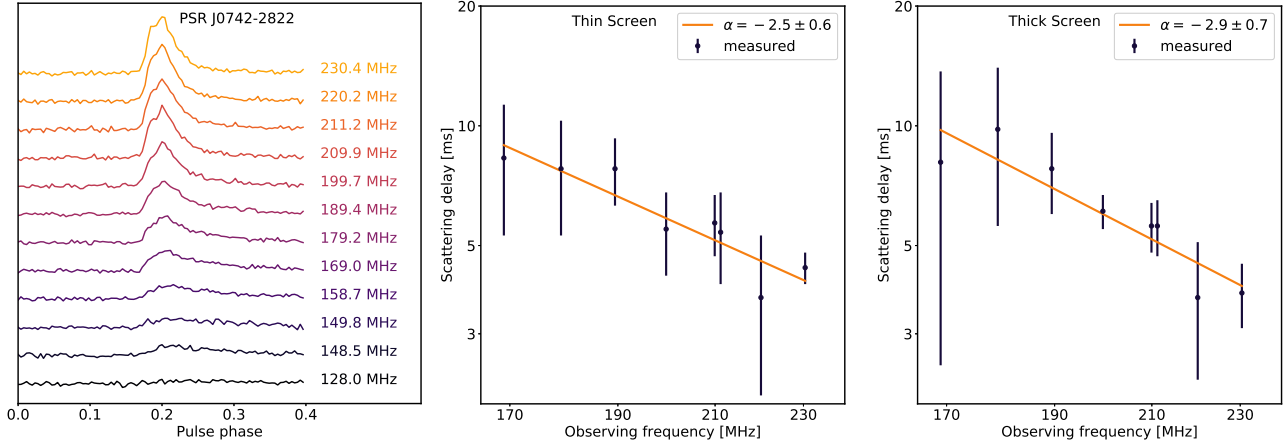


Figure 3. Left: Measured pulse profiles of J0742–2822 as seen in coherently summed data, zoomed in on the pulse phase containing the signal. The bandwidth in each subband is 1.28 MHz. Below an observing frequency of 148.5 MHz the pulsar is scattered beyond detection while above 230 MHz RFI prevented us from coherently summing the array. Middle and right: Measured scattering delay vs. observing frequency for J0742–2822 using both a thin and a thick screen model for scattering, as described in the text. The yellow line in both plots is a power law fit of the form $\tau \propto \nu^\alpha$. In the fitting procedure we omitted the measurements below 169 MHz because of low SNR and, hence, unreliable scattering delays.

More realistic models typically have a shallower rise time and a longer exponential tail, corresponding to different peak positions. Williamson (1972) showed that for a thick scattering screen, the PBF at small times t , i.e. during the rise time up until shortly after the peak of the emission, is given by

$$g_1(t) = \left(\frac{\pi\tau}{4t^3}\right)^{1/2} \exp\left[-\frac{\pi^2\tau}{16t}\right]. \quad (2)$$

The shape of the decaying tail can be described by an exponential, $e^{-t/\tau}$, similar to $g_0(t)$.

To evaluate the quality of the deconvolution procedure we make use of the figures of merit (FOM) defined in Bhat et al. (2003). In particular these are the positivity f_r (the PBF should not over-subtract the flux), the symmetry Γ (the deconvolved pulse should not show a residual scattering tail) and the consistency of the residuals with the off-pulse rms indicated by N_r (the relative number of bins that are within three standard deviations of the off-pulse region) and σ_r (the ratio of the rms in the CLEANed window to the rms in the off-pulse region). For convenience we summarize the definitions of each parameter in Appendix A. The deconvolution procedure should minimize f_r and Γ , while maximizing N_r and achieving $\sigma_r \sim 1$. It is important to note that the absolute numbers of parameters Γ , N_r and σ_r do not allow for a meaningful assessment which scattering model provides a better fit. They merely serve to find the best fit τ as illustrated in Figure 8.

We use f_r also to estimate the uncertainties of our measured τ . In a least-squares fitting routine, the minimum of the reduced chi-square statistic, χ_{red}^2 , indicates the best fit model. The parameter range for which χ_{red}^2

is unity above that minimum indicates the uncertainty of the measured parameter. Similarly, we use the range in τ for which f_r is unity above the best fit model to estimate our uncertainties. In general the absolute number of this parameter carries little information. It is only in comparison to another model where a lower value of f_r indicates a better fit. Similarly, we also compute a reduced chi-square value, χ_{nCC}^2 , from our best-fit model in order to have a relative measure for the goodness of fit between the thick screen model and the thin screen model. In this context we use the number of pulse phase bins in which CLEAN components were subtracted, nCC , as an estimate for the number of degrees of freedom³. We emphasize that χ_{nCC}^2 computed in this way is merely another figure of merit that can be employed to prefer one model for scattering over another.

3.1. PSR J0742–2822

Using the above method, we analyzed the J0742–2822 data by adopting a PBF form as in Eq. 1 and Eq. 2. We have performed this for each subband separately; the resultant scattering delays τ and associated FOM are summarized in Table 3. Overall, the positivity parameter f_r and the parameter χ_{nCC}^2 are lower for the thin screen model than the thick screen one indicating that a thin screen geometry is a better representation of the data.

³ The total number of CLEAN components is a strong function of the loop gain, the S/N of the pulse, and the time resolution of the data; it is typically of the order of a few thousand.

Table 3. Measured scattering delays for J0742–2822

| Frequency | | Thin screen | | | | | | | Thick screen | | | | | | |
|-----------|-------------|-------------|-------|------------|----------|----------------|-------|--|--------------|-------|-------|------------|----------|----------------|-------|
| [MHz] | τ [ms] | f_r | N_r | σ_r | Γ | χ^2_{nCC} | nCC | | τ [ms] | f_r | N_r | σ_r | Γ | χ^2_{nCC} | nCC |
| 230.40 | 4.4(4) | 0.77 | 0.19 | 1.95 | 0.22 | 42 | 17 | | 3.8(7) | 0.55 | 0.19 | 1.25 | 0.31 | 112 | 6 |
| 220.16 | 3.7(16) | 0.12 | 0.18 | 1.23 | 0.55 | 29 | 21 | | 3.7(14) | 0.63 | 0.18 | 1.13 | 0.54 | 89 | 7 |
| 211.20 | 5.4(14) | 0.12 | 0.18 | 0.89 | 0.31 | 32 | 18 | | 5.6(9) | 0.20 | 0.19 | 0.89 | 0.19 | 91 | 6 |
| 209.92 | 5.7(9) | 0.30 | 0.19 | 1.23 | 0.23 | 32 | 17 | | 5.6(8) | 0.62 | 0.19 | 0.97 | 0.08 | 110 | 5 |
| 199.68 | 5.5(13) | 0.11 | 0.19 | 1.57 | 0.02 | 45 | 18 | | 6.1(6) | 0.70 | 0.19 | 1.13 | −0.19 | 129 | 6 |
| 189.44 | 7.8(15) | 0.05 | 0.20 | 2.03 | 0.29 | 40 | 14 | | 7.8(18) | 0.14 | 0.19 | 1.00 | 0.29 | 172 | 3 |
| 179.20 | 7.8(25) | 0.02 | 0.19 | 0.90 | 0.50 | 36 | 14 | | 9.8(42) | 0.37 | 0.20 | 0.91 | −0.29 | 147 | 3 |
| 168.96 | 8.3(30) | 0.03 | 0.19 | 1.16 | 0.22 | 46 | 15 | | 8.1(56) | 0.05 | 0.19 | 1.03 | 0.63 | 129 | 5 |
| α | | −2.5(6) | | | | | | | −2.9(7) | | | | | | |

NOTE—Numbers in brackets indicate the uncertainty in the last digit.

Table 4. Measured scattering delays for the Vela Pulsar

| Frequency | | Thin screen | | | | | | | Thick screen | | | | | | |
|-----------|----------------|----------------|-------|------------|----------|----------------|-------|--|----------------|-------|-------|------------|----------|----------------|-------|
| [MHz] | τ [ms] | f_r | N_r | σ_r | Γ | χ^2_{nCC} | nCC | | τ [ms] | f_r | N_r | σ_r | Γ | χ^2_{nCC} | nCC |
| 256 | 14.1 ± 1.7 | 1.6 | 0.26 | 1.66 | 0.33 | 21 | 5 | | 11.4 ± 2.5 | 0.53 | 0.28 | 1.65 | 0.36 | 21 | 5 |
| 210 | 31.2 ± 8.1 | 0.2 | 0.31 | 1.24 | 0.86 | 22 | 5 | | 32.6 ± 4.7 | 0.28 | 0.31 | 1.46 | 1.13 | 38 | 3 |
| α | | -4.0 ± 1.5 | | | | | | | -5.0 ± 1.5 | | | | | | |

The middle and right panels of Figure 3 depict the measured scattering delays as a function of frequency for both the thin and thick screen models, respectively. Also shown are power law fits of the form $\tau \propto \nu^\alpha$. For the thin screen model we obtain $\alpha = -2.5 \pm 0.6$, which is well in agreement with the measurements of Lewandowski et al. (2015, $\alpha = -2.52 \pm 0.3$) but lower than those of Geyer et al. (2017) who measure $\alpha = -3.8 \pm 0.4$. The use of the thick screen model, yields a slightly higher $\alpha = -2.9 \pm 0.7$, which agrees with the thin-screen-estimate within the uncertainties.

3.2. The Vela Pulsar

In the lowest band of our observations, the effect of scatter broadening becomes too large to enable a detection of the pulsar, and the detection in the two bands centered at 164.5 MHz and 179.8 MHz is only marginal (Figure 1). Therefore, we restrict our analysis to the highest two bands, centered on 210.56 MHz and 256.64 MHz. The frequency scalings as indicated by the measured delays (Table 4) are $\alpha = -4.0 \pm 1.5$ (thin screen model) and $\alpha = -5.0 \pm 1.5$ (thick screen model). The FOM also listed in Table 4 do not indicate a clear trend for which model reproduces the observations better. The post-CLEANing residuals are similar in their noise characteristics (indicated by σ_r and N_r)

and the skewness Γ is also very similar between the models. Both the f_r -parameter and χ^2_{nCC} indicate that the thick screen model is a better representation of the observations at 256 MHz, while at 210 MHz the thin screen model provides a better fit.

3.3. The Crab Pulsar

The complexity of the pulse profile of the Crab pulsar and the degree of scattering at MWA frequencies render the analysis of average profiles unsuitable for the estimation of its scattering delays. The scattering tail extends well beyond the pulsar period at the lower frequencies.

The Crab pulsar is known for giant pulses exceeding the flux density of its regular pulses by orders of magnitude. Therefore, we can use a single giant pulse to study the effects of the ISM on the Crab pulsar’s emission. Intrinsically, giant pulses are of $\sim \mu\text{s}$ time duration (e.g. Bhat et al. 2008; Popov & Stappers 2007), so can be treated as impulsive signals given the native resolution of our VCS recordings (100 μs). Hence, the problem of an unknown intrinsic pulse shape does not apply to giant pulses and a normal least-squares fitting routine can be applied when fitting scattering models. We tried

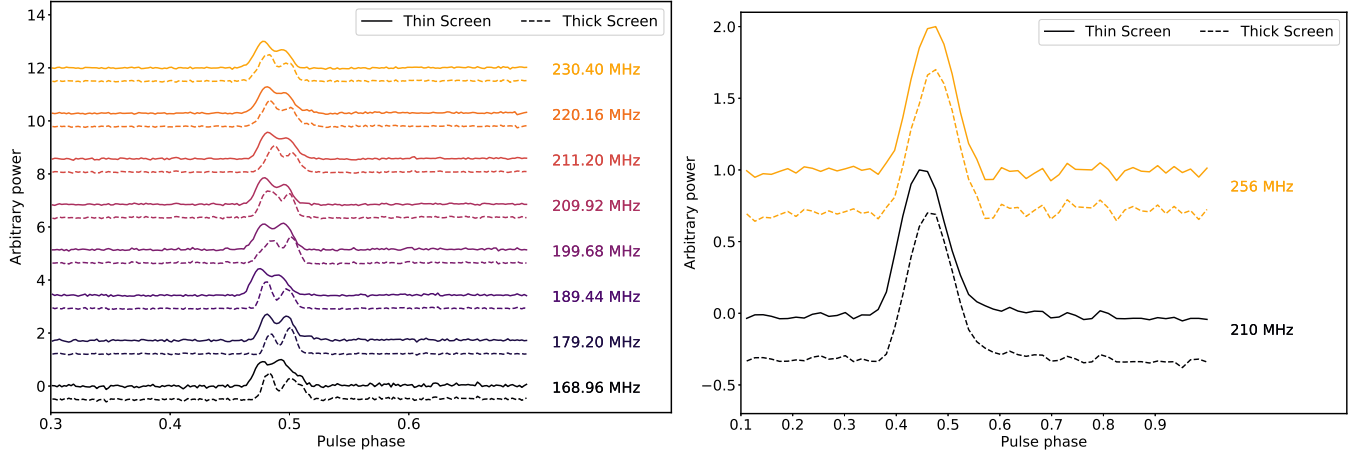


Figure 4. Reconstructed pulse profiles for PSR J0742–2822 (left) and the Vela pulsar (right). The solid lines show the results from using the thin screen model while the dashed lines show those from the thick screen model. The different observing bands are color coded.

Table 5. Measured scattering delays for the Crab Pulsar and implied frequency scalings

| Frequency [MHz] | Square law structure function | | | | | | Fully diffractive Kolmogorov turbulence | | | | | |
|--------------------|-------------------------------|-----------------------|-------------|-----------------------|---------------|-----------------------|---|-----------------------|-------------|-----------------------|-------------|-----------------------|
| | Thin | | Thick | | Modified thin | | Thin | | Thick | | Double thin | |
| | τ [ms] | χ^2_{red} | τ [ms] | χ^2_{red} | τ [ms] | χ^2_{red} | τ [ms] | χ^2_{red} | τ [ms] | χ^2_{red} | τ [ms] | χ^2_{red} |
| 121 | 58(1) | 0.97 | 44.9(9) | 0.85 | 40(2) | 0.95 | 47(13) | 1.26 | 46(2) | 1.16 | 47(13) | 1.26 |
| 165 | 18.3(2) | 1.06 | 12.8(1) | 1.08 | 11.9(2) | 1.01 | 14(2) | 1.44 | 13.2(3) | 1.47 | 14(2) | 1.52 |
| 210 | 8.4(1) | 1.16 | 5.72(6) | 1.01 | 4.66(9) | 1.08 | 6.4(9) | 1.58 | 6.75(7) | 1.40 | 6.3(9) | 1.84 |
| α | −3.5(1) | | −3.8(2) | | −3.9(1) | | −3.7(2) | | −3.6(3) | | −3.7(2) | |

both PBF forms in Equations 1 and 2 and, additionally, also fit a modified exponential function defined as

$$g_2(t) = t^\gamma \exp\left[-\frac{t}{\tau}\right] u(t), \quad (3)$$

where γ is a free parameter in the range 0–1 describing the rise time of the pulse; $u(t)$ is as defined for Equation 1. Both Karuppusamy et al. (2012) and Ellingson et al. (2013) have made use of this PBF and found that this functional form fits their data better at low frequencies. We restrict our analysis to the lower three bands where the signal-to-noise ratio (SNR) is highest (Fig. 1). The data and associated fits are shown in the left column of Figure 5 and the measured scattering delays along with the reduced χ^2_{red} values are summarized in Table 5.

Figure 5 (right column) also contains the results of numerical fits where we employed PBFs that are based on a fully diffractive Kolmogorov model of turbulence (e.g. Lambert & Rickett 1999). This work is motivated by the fact that none of the above three models (Eqs. 1, 2, and 3), which are based on the assumption of a square-law structure function of the ISM, fits the data

well across all three bands. Moreover, all three models assume that the scattering occurs in only one location along the path. For the Crab pulsar it has been suggested there may be two distinct contributing scattering locations, namely material within the Crab nebula itself and the ISM between Earth and the pulsar (Vandenberg 1976). Therefore, we are motivated to explore a set of models in which the scattering occurs at multiple locations along the ray path. In particular, we investigate the case in which the scattering occurs on multiple thin screens. It may be shown that the multiple thin screen geometry gives rise to a scattering kernel whose shape is the convolution of the scattering kernels of the two screens individually.

The scattering delays that we measure for each of the six models indicate a frequency scaling $-4.0 < \alpha < -3.4$ (Table 5). This is slightly steeper than but consistent with the results of, e.g., Meyers et al. (2017); Eftekhari et al. (2016), and in excellent agreement with a global scattering index $\langle \alpha \rangle = -3.9 \pm 0.2$ determined by Bhat et al. (2004). The parameter γ in Eq. 3 evaluates to 0.18 ± 0.02 at all frequencies. This is in good agreement with the values found by Karuppusamy et al.

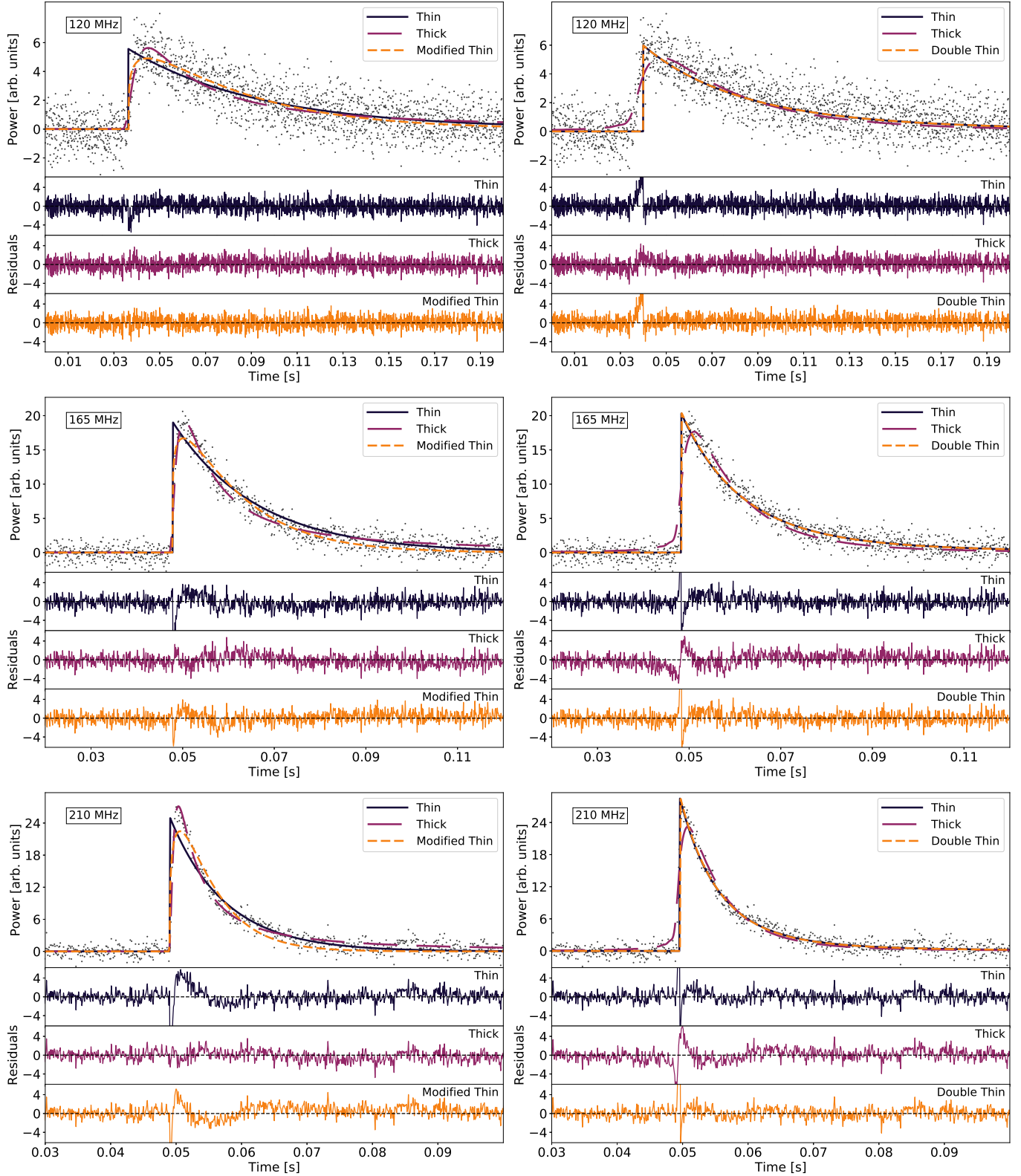


Figure 5. Scattered profiles of one particular giant pulse of the Crab at 120 MHz (top row), 165 MHz (middle row), 210 MHz (bottom row) with different scattering models overplotted and their respective residuals (color coded according to the model below each pulse). The left column shows fits using the canonical models of thin, thick and modified thin models for the scattering screen while the right column show fits for fully diffractive models of Kolmogorov turbulence. None of the models explains the observed profile sufficiently well across all frequencies. Note the different time scales at the different frequencies.

Table 6. Residual dispersion smearing time across 10 kHz at 120 MHz and 230 MHz

| Pulsar | DM | $\tau_{\text{disp}} [\text{ms}]$ | |
|------------|-----------------------|----------------------------------|---------|
| | $[\text{pc cm}^{-3}]$ | 120 MHz | 230 MHz |
| J0534+2200 | 56.7 | 2.72 | 0.39 |
| J0742–2822 | 73.7 | 3.54 | 0.50 |
| J0835–4510 | 67.9 | 3.26 | 0.46 |

(2012) and lower but still within three standard deviations of the results found by Ellingson et al. (2013).

4. DISCUSSION

4.1. PSR J0742–2822

The work of Johnston et al. (1998) suggested that the interstellar scattering along this line of sight is dominated by a thin screen located within the Gum Nebula. Our measurements are well in line with this notion as the FOM (Table 3) favor the thin screen model over the thick screen one. For all eight frequency bands considered in the analysis, both f_r and χ^2_{nCC} are lower for the thin screen model than the thick screen one, indicating a better fit to the data. The thin screen model yields a scaling index $\alpha = -2.5 \pm 0.6$ that is in agreement with previous work (e.g. Lewandowski et al. 2015). However, the measured scattering delays τ and the frequency scaling $\alpha = -2.9 \pm 0.7$ as obtained from assuming a thick screen model agree with the thin screen estimates within one standard deviation.

One can also compare the recovered deconvolved pulse shapes between models with those obtained at higher frequencies. We show our profiles in Fig. 4 (left) which hint at a double-peaked pulse regardless of the assumed underlying model for scattering. Similar double peaked profiles with matching component separations are evident at higher frequencies for this pulsar (e.g. Kramer 1994; Zhao et al. 2017, and references therein). However, as the signal-to-noise ratio (SNR) in the individual subbands is low, these reconstructed pulse shapes should be considered as first order estimates only. The measured scattered profiles (Fig. 3, left), on the other hand, are very reliable as they were constructed from about 1800 individual pulses.

Furthermore, we can consider the scintillation properties at higher frequencies implied by a certain frequency scaling. For diffractive scintillation, the decorrelation bandwidth $\Delta\nu_d$ is related to the scatter broadening time τ via the relation $\Delta\nu_d = C/(2\pi\tau)$, where C is of order unity (Lambert & Rickett 1999, C ranges from 0.65 to 1.2 depending on assumed geometry and underlying den-

sity spectrum). For PSR J0742–2822 an $\alpha = -2.5$ (or $\alpha = -2.9$ for the thick screen) would predict a decorrelation bandwidth $\Delta\nu_d \approx 0.1$ MHz ($\Delta\nu_d \approx 0.2$ MHz, thick screen) at 4.8 GHz that is only about an order of magnitude lower than what has been measured by Johnston et al. (1998) at that frequency ($\Delta\nu_d = 8.83$ MHz). Considering the time variability of scintillation and the uncertainties of our measurements our results are well in line with these earlier findings.

4.2. The Vela Pulsar

Similar to PSR J0742–2822, it has been speculated that the Gum Nebula is the dominant source of scattering along the line of sight to the source (Backer 1974), favoring the model of a thin scattering screen over a thick one. The measurements we present in Table 4, however, are inconclusive as neither the frequency scaling nor the FOM enable us to critically distinguish between the two interstellar scattering models used in the analysis. To a large degree this is caused by the limited amount of data points (the SNR was high enough in only the highest two out of five subbands) and the fact that we are limited in both time and frequency resolution (100 μs and 10 kHz, respectively) leading to (i) the inability to recover small scale pulse structure (e.g. Johnston et al. 2001, for the Vela pulsar); and (ii) residual dispersive smearing (Table 6). The overall effect is that the recovered, deconvolved pulse shapes are a low-resolution estimate of the intrinsic pulse shapes, hindering discrimination between scattering models (Fig. 4, right). With higher time and frequency resolution one could compare the recovered pulse shapes with those observed at higher frequencies, providing a further aspect against which to compare the goodness of fit.

Within their respective uncertainties, both the thick and the thin screen model yield a scaling index α that is in agreement with previous work (e.g. Lewandowski et al. 2015; Johnston et al. 1998), which fits into the standard picture of Kolmogorov turbulence. However, one can again consider the implications of the scaling indices for the decorrelation bandwidth at higher frequencies. For the Vela a frequency scaling of $\alpha = -5.0$ would indicate a decorrelation bandwidth $\Delta\nu_d \approx 1$ MHz at an observing frequency of 2.3 GHz, while a scaling $\alpha = -4.0$ would yield $\Delta\nu_d \approx 70$ kHz. The latter is in good agreement with $\Delta\nu_d = 66$ kHz measured by Gwinn et al. (2000). Thus, there is a preference for a thin screen scattering geometry along the line of sight to the Vela pulsar.

4.3. The Crab

None of the models that we fitted to the brightest giant pulse in our dataset reproduce the observed pulse

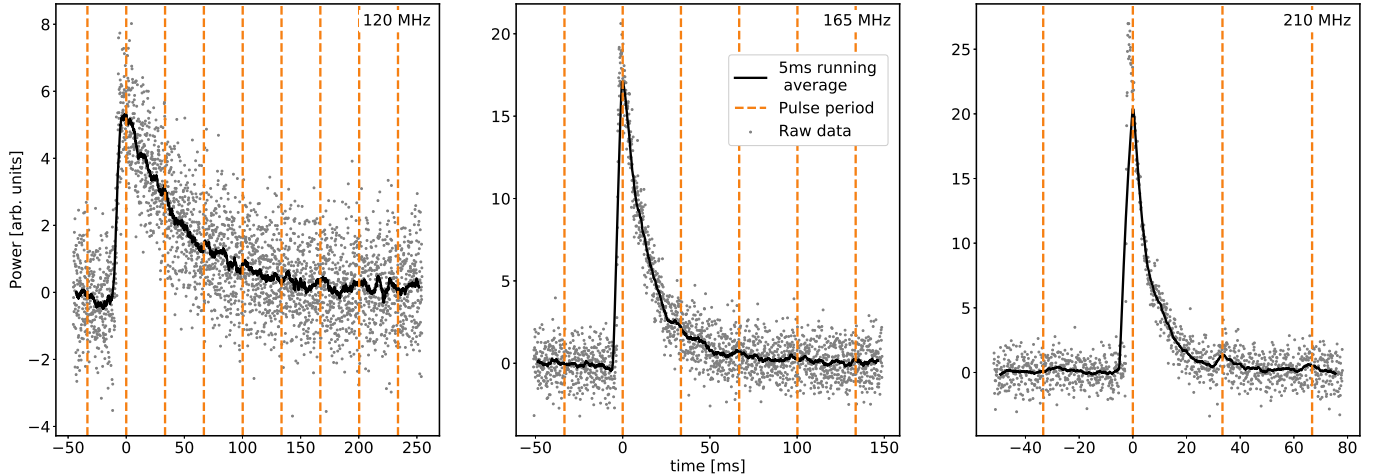


Figure 6. Raw data (gray dots) and a five milliseconds running average thereof (black line) of the Crab giant pulse fitted in Figure 5. The vertical yellow dashed lines indicate time steps of one pulse period of the Crab (≈ 33.3 ms) relative to the peak of the averaged profile. Note how the power in the scattering tail is increased by pulses succeeding the giant pulses, ultimately influencing the results of the fitting procedure. Also note the different time ranges at the different central frequencies of 120 MHz (left), 165 MHz (center), and 210 MHz (right).

shapes well across all three frequency bands (Fig. 5). They generally fail to capture the rise times correctly, with the model for a thick scattering screen describing the leading edge best, i.e. the residuals show nearly no deviation from flatness in this particular time range of the pulse. However, this model, like all others, does not reproduce the shape of the scattering tail in a way that the residuals show no systematic offset from zero. At a central frequency of 165 MHz the model for a thick scattering screen decays too steeply, i.e. it does not account for all the power still present right after the peak of the pulse, while at 210 MHz this model predicts more power at later times in the tail than is actually present. The latter might indicate the presence of an inner scale of turbulence as observed by, e.g., [Rickett et al. \(2009\)](#).

Similar to the analytic models, none of the numerical models we employed appropriately characterize the immediate rise time of the pulse. Compared to the analytic models, the residuals of the single thin and double thin models are, however, somewhat flatter both right after the peak of the pulse and at later times in the scattering tail. We interpret this as an indication that compared to the analytical models, the numerical models for thin screens better account for both the small scale scattering structures as well as the larger scale structures.

The fitting results of both the analytic and the numerical approach are strongly influenced by the fact that the scattering tail extends beyond a single pulse period. This becomes evident in Figure 6 where we plot the raw data in all three subbands alongside with a five millisecond running average. In all three subbands one can identify an increase in power in the scattering tail at

intervals equal to the pulse period. We interpret these peaks as pulses succeeding the giant pulse, ultimately leading to a measurement of the scatter broadening time that is larger than that induced by the ISM.

Similarly, the influence of subsequent pulses makes it virtually impossible to distinguish between a simple exponentially decaying scattering tail and one that decays slower as is expected for Kolmogorov turbulence ([Lambert & Rickett 1999](#)).

5. SUMMARY & CONCLUSIONS

We observed the three pulsars J0534+2200 (the Crab pulsar), J0742–2822, and J0835–4510 (the Vela pulsar) across the entire frequency range available with the MWA (80–300 MHz). We employed both analytical and numerical models for interstellar scattering to measure the pulse scatter broadening times induced by the ISM between frequencies of 148 MHz and 256 MHz. Based on these measurements we were able to estimate the frequency scaling of interstellar scattering implied by the different models which generally agree within their uncertainties despite the fact that the measured τ differ significantly between models. We find that both a thin and a thick screen model are consistent with our data, albeit a preference for a thin screen geometry for both J0742–2822 and J0835–4510. The thin screen models imply frequency scalings $\alpha = -2.5 \pm 0.6$ and $\alpha = -4.0 \pm 1.5$ for J0742–2822 and the Vela pulsar, respectively. These numbers are in agreement with previous publications (e.g. [Lewandowski et al. 2015](#)). In the case of the Crab pulsar our data indicate that none of our employed models represents the data accurately

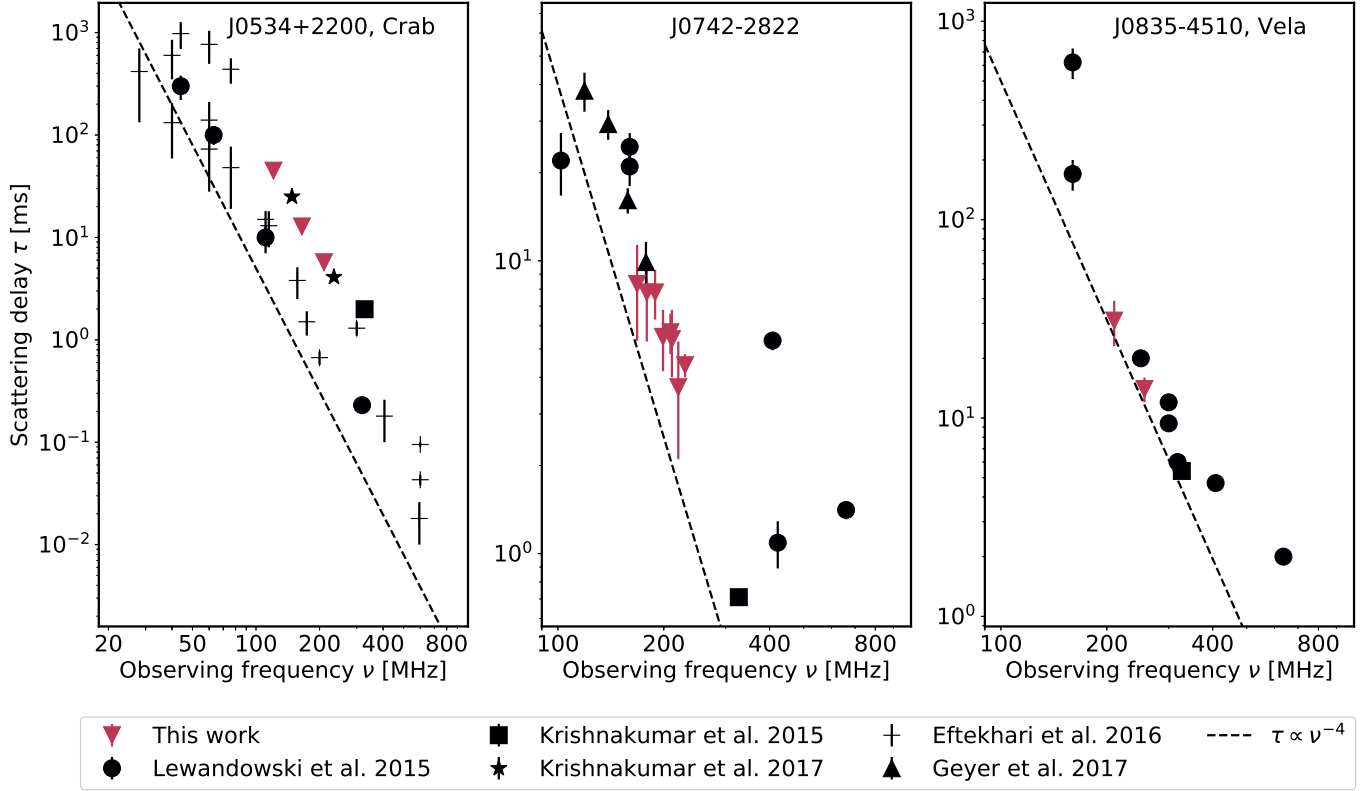


Figure 7. Scattering delays below an observing frequency $\nu < 1000$ MHz as found in the literature (black circles, squares, stars, and triangles) and our measured values (red triangles) for J0534+2200 (left, from thick screen model), J0742–2822 (middle, from thin screen model) and J0835–4510 (right, from thin screen model). All values from the literature are based on the assumption of a single thin scattering screen (Eq 1), with the exception of the data from Eftekhari et al. (2016) who used the modified thin screen model (Eq. 3). The dashed line indicates the canonical relation $\tau \propto \nu^{-4}$.

across all observed frequencies, with the model for a thick scattering screen fitting the rise times of the analyzed giant pulse best. The frequency scaling implied by this model is $\alpha = -3.8 \pm 0.2$. Overall, the spectral scaling indices we measure are all shallower than what is expected for pure Kolmogorov turbulence ($\alpha = -4.4$). The existence of an inner scale of turbulence could at least partially explain this discrepancy (e.g. Rickett et al. 2009; Bhat et al. 2004).

The scattering delays that we measured in these short, multi-band, single epoch observations with the MWA fit very well into what has been measured previously (Figure 7). In these previous works, the large scatter of the measured delays at similar frequencies is most likely caused by combining data from (i) separate observations spanning long time ranges, (ii) multiple dissimilar telescopes, and (iii) varying techniques to measure the scattering delay. Effectively, this will not only affect the measured delays but also the implied frequency scaling index of pulsar scattering, α . In this work, we accomplished these measurements from relatively short, single-epoch observations with the MWA alleviating all of the above difficulties. This is a testimony to the sensi-

tivity and flexibility of the MWA and it underscores the importance of pulsar studies at low radio frequencies.

We thank the two anonymous referees for insightful reviews and for several comments that helped to improve the content and presentation in this paper. FK acknowledges funding through the Australian Research Council grant DP140104114 and from the Swedish Research Council. NDRB acknowledges the support from a Curtin Research Fellowship (CRF12228). The authors acknowledge the contribution of an Australian Government Research Training Program Scholarship in supporting this research. This scientific work makes use of the Murchison Radio-astronomy Observatory, operated by CSIRO. We acknowledge the Wajarri Yamatji people as the traditional owners of the Observatory site. Support for the operation of the MWA is provided by the Australian Government (NCRIS), under a contract to Curtin University administered by Astronomy Australia Limited. We acknowledge the Pawsey Supercomputing Centre which is supported by the Western Australian and Australian Governments. Parts of this research were

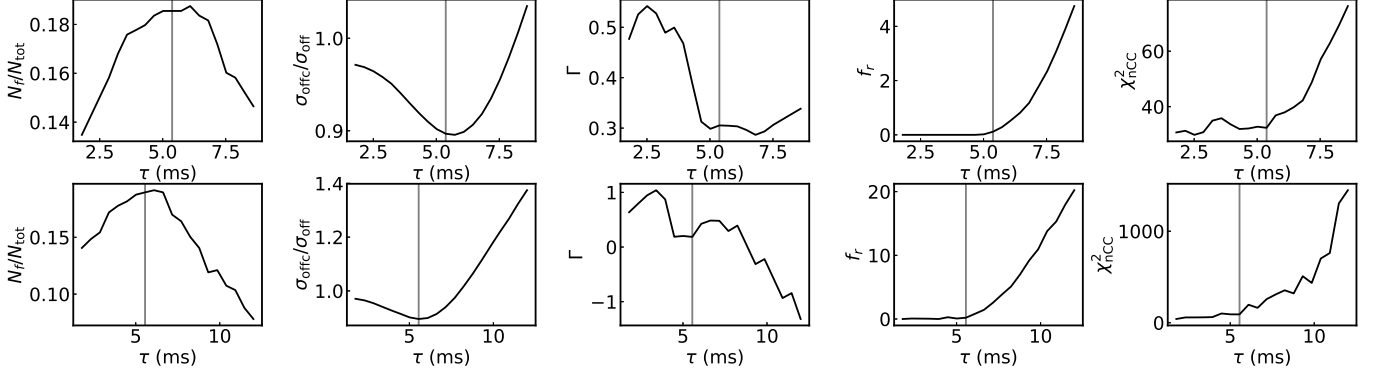


Figure 8. Examples of the collection of figures of merit employed to determine the best fit model. Shown are the FOMs as computed for PSR J0742–2822 at an observing frequency of 211.2 MHz. Top row: FOMs for thin screen model (Eq. 1); bottom row: FOMs for thick screen model (Eq. 2). The gray horizontal lines indicate the value of τ that was taken to be the best fit value.

conducted by the Australian Research Council Centre of Excellence for All-sky Astrophysics (CAASTRO), through project number CE110001020.

Software: PSRCHIVE, DSPSR, PYTHON, MATLAB

Facilities: MWA

APPENDIX

A. FIGURES OF MERIT

Here we summarize the definitions of the FoM as defined in (Bhat et al. 2003). An example of how we chose the best fit model is shown in Fig. 8.

The parameter f_r is defined as

$$f_r = \frac{1}{N\sigma_{off}^2} \sum_{i=1}^N [\Delta y(t_i)]^2 U_{\Delta y},$$

where $U_{\Delta y}$ is the unit step function defined such that

$$U_{\Delta y} = \begin{cases} 1 & \text{if } (\Delta y(t_i) + 1.5\sigma_{off}) < 0, \\ 0 & \text{otherwise,} \end{cases}$$

and N is the total number of time bins t_i during which the pulse is ‘on’. σ_{off} denotes the off-pulse rms noise while the parameter $\Delta y(t_i)$ denotes the value of time bin t_i in the CLEAN residual (i.e. the residual profile after subtraction of all CLEAN components). Effectively, f_r is a measure for positivity, i.e. how much oversubtraction occurs given the CLEANed pulse of a certain model.

$N_r = N_f/N_{tot}$ denotes the relative number of points N_f that satisfy $|y_i - \langle y_{off} \rangle| \leq 3\sigma_{off}$, where $\langle y_{off} \rangle$ denotes the off-pulse mean signal and N_{tot} are the total number of points in the profile.

$\sigma_r = \sigma_{offc}/\sigma_{off}$ is the ratio between the rms of the residual after deconvolution and the off-pulse rms in the scattered profile. It is a relative measure for how noise-like the residual of the deconvolved pulse is.

The skewness Γ is a measure for the symmetry of the CLEANed profile and is computed as

$$\Gamma = \frac{\langle t^3 \rangle}{\langle t^2 \rangle^{3/2}}, \text{ with}$$

$$\langle t^n \rangle = \frac{\sum_{i=1}^{n_c} (t_i - \bar{t})^n C_i}{\sum_{i=1}^{n_c} C_i},$$

$$\bar{t} = \frac{\sum_{i=1}^{n_c} t_i C_i}{\sum_{i=1}^{n_c} C_i}.$$

Here, the summation parameter $i = 1, \dots, n_c$ runs through all CLEAN components of amplitudes C_i and associated times t_i .

REFERENCES

- Backer, D. C. 1974, *ApJ*, 190, 667
- Bhat, N. D. R., Cordes, J. M., Camilo, F., Nice, D. J., & Lorimer, D. R. 2004, *ApJ*, 605, 759
- Bhat, N. D. R., Cordes, J. M., & Chatterjee, S. 2003, *ApJ*, 584, 782
- Bhat, N. D. R., Tingay, S. J., & Knight, H. S. 2008, *ApJ*, 676, 1200
- Bhat, N. D. R., Wayth, R. B., Knight, H. S., et al. 2007, *ApJ*, 665, 618
- Braithwaite, J. 2015, *MNRAS*, 450, 3201
- Briskin, W. F., Macquart, J.-P., Gao, J. J., et al. 2010, *ApJ*, 708, 232
- Cordes, J. M., & Lazio, T. J. W. 2001, *ApJ*, 549, 997
- Cordes, J. M., Shannon, R. M., & Stinebring, D. R. 2016, *ApJ*, 817, 16
- Dodson, R., Legge, D., Reynolds, J. E., & McCulloch, P. M. 2003, *ApJ*, 596, 1137
- Eftekhari, T., Stovall, K., Dowell, J., Schinzel, F. K., & Taylor, G. B. 2016, *ApJ*, 829, 62
- Ellingson, S. W., Clarke, T. E., Craig, J., et al. 2013, *ApJ*, 768, 136
- Geyer, M., & Karastergiou, A. 2016, *MNRAS*, 462, 2587
- Geyer, M., Karastergiou, A., Kondratiev, V. I., et al. 2017, *MNRAS*, 470, 2659
- Gwinn, C. R., Britton, M. C., Reynolds, J. E., et al. 2000, *ApJ*, 531, 902
- Högbom, J. A. 1974, *A&AS*, 15, 417
- Hotan, A. W., van Straten, W., & Manchester, R. N. 2004, *PASA*, 21, 302
- Johnston, S., Nicastro, L., & Koribalski, B. 1998, *MNRAS*, 297, 108
- Johnston, S., van Straten, W., Kramer, M., & Bailes, M. 2001, *ApJL*, 549, L101
- Karuppusamy, R., Stappers, B. W., & Lee, K. J. 2012, *A&A*, 538, A7
- Keith, M. J., Coles, W., Shannon, R. M., et al. 2013, *MNRAS*, 429, 2161
- Kramer, M. 1994, *A&AS*, 107, 527
- Krishnakumar, M. A., Joshi, B. C., & Manoharan, P. K. 2017, *ApJ*, 846, 104
- Lam, M. T., Cordes, J. M., Chatterjee, S., et al. 2016, *ApJ*, 821, 66
- Lambert, H. C., & Rickett, B. J. 1999, *ApJ*, 517, 299
- Lewandowski, W., Kowalińska, M., & Kijak, J. 2015, *MNRAS*, 449, 1570
- Line, J. L. B., Webster, R. L., & Pindor, B. 2016, *MNRAS*, astro-ph/1611.05534
- Manchester, R. N., Hobbs, G. B., Teoh, A., & Hobbs, M. 2005, *AJ*, 129, 1993
- Meyers, B. W., Tremblay, S. E., Bhat, N. D. R., et al. 2017, *ApJ*, 851, 20
- Mitchell, D. A., Greenhill, L. J., Wayth, R. B., et al. 2008, *IEEE Journal of Selected Topics in Signal Processing*, 2, 707
- Ord, S. M., Crosse, B., Emrich, D., et al. 2015, *PASA*, 32, e006
- Pen, U.-L., & Levin, Y. 2014, *MNRAS*, 442, 3338
- Popov, M. V., & Stappers, B. 2007, *A&A*, 470, 1003
- Rickett, B., Johnston, S., Tomlinson, T., & Reynolds, J. 2009, *MNRAS*, 395, 1391
- Rickett, B. J. 1990, *ARA&A*, 28, 561
- Sault, R. J., Hamaker, J. P., & Bregman, J. D. 1996, *A&AS*, 117, 149
- Stinebring, D. R., McLaughlin, M. A., Cordes, J. M., et al. 2001, *ApJL*, 549, L97
- Taylor, G. B., Ellingson, S. W., Kassim, N. E., et al. 2012, *Journal of Astronomical Instrumentation*, 1, 1250004
- Tingay, S. J., Goeke, R., Bowman, J. D., et al. 2013, *PASA*, 30, e007
- Tremblay, S. E., Ord, S. M., Bhat, N. D. R., et al. 2015, *PASA*, 32, e005
- van Haarlem, M. P., Wise, M. W., Gunst, A. W., et al. 2013, *A&A*, 556, A2
- van Straten, W., & Bailes, M. 2011, *PASA*, 28, 1
- van Straten, W., Demorest, P., & Osłowski, S. 2012, *Astronomical Research and Technology*, 9, 237
- Vandenberg, N. R. 1976, *ApJ*, 209, 578
- Walker, M. A., Melrose, D. B., Stinebring, D. R., & Zhang, C. M. 2004, *MNRAS*, 354, 43
- Williamson, I. P. 1972, *MNRAS*, 157, 55
- Xu, S., & Zhang, B. 2017, *ApJ*, 835, 2
- Yao, J. M., Manchester, R. N., & Wang, N. 2017, *ApJ*, 835, 29
- You, X. P., Hobbs, G., Coles, W. A., et al. 2007, *MNRAS*, 378, 493
- Zhao, R.-S., Wu, X.-J., Yan, Z., et al. 2017, *ApJ*, 845, 156